ACS NANO

www.acsnano.org

ARTICLE

Flash-Thermal Shock Synthesis of Single Atoms in Ambient Air

Dong-Ha Kim,[▽] Jun-Hwe Cha,[▽] Sanggyu Chong, Su-Ho Cho, Hamin Shin, Jaewan Ahn, Dogyeong Jeon, Jihan Kim, Sung-Yool Choi,* and Il-Doo Kim*

Cite This: *ACS Nano* 2023, 17, 23347−23358

Read Online

ACCESS | Metrics & More | Article Recommendations | Supporting Information

ABSTRACT: **Single-atom catalysts feature interesting catalytic activity toward applications that rely on surface reactions such as electrochemical energy storage, catalysis, and gas sensors. However, conventional synthetic approaches for such catalysts require extended periods of high-temperature annealing in vacuum systems, limiting their throughput and increasing their production cost. Herein, we report an ultrafast flash-thermal shock (FTS)-induced annealing technique (temperature > 2850 °C, <10 ms duration, and ramping/cooling rates of ∼10^5 K/s) that operates in an ambient-air environment to prepare single-atom-stabilized N-doped graphene. Melamine is utilized as an N-doping source to provide thermodynamically favorable metal−nitrogen bonding sites, resulting in a uniform and high-density atomic distribution of single metal atoms. To demonstrate the practical utility of the single-atom-stabilized N-doped graphene produced by the FTS method, we showcased their chemiresistive gas sensing capabilities and electrocatalytic activities. Overall, the air-ambient, ultrafast, and versatile (e.g., Co, Ni, Pt, and Co−Ni dual metal) FTS method provides a general route for high-throughput, large area, and vacuum-free manufacturing of single-atom catalysts.**

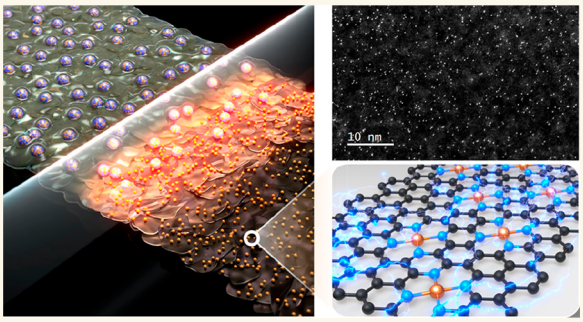

KEYWORDS: *intense pulsed light, photothermal effect, ambient-air process, single-atom, N-doping*

Single-atom catalysts (SACs) incorporate characteristics of both homogeneous and heterogeneous catalysts with their maximized coordination structures to provide an optimal catalytic environment for surfaced-limited chemical reactions.[1,2] SACs have been explored for catalytic reactions such as CO oxidation,[3] oxygen reduction reaction (ORR),[4] hydrogen evolution reaction,[5] and gas sensing,[6−8] exhibiting improved performances compared to conventional heterogeneous catalysts given the same mass loading.

It is generally understood that individual atoms are thermodynamically unstable due to high free energy of the system. As a result, they can randomly migrate and form nanoclusters or nanoparticles at elevated temperatures.[1] Therefore, to effectively prepare SACs, high-energy processes are often necessary to overcome the thermodynamic instability in a top-down approach. In addition, bottom-up methods based on chemical reactions are suggested without any high temperature or atmospheric control involved.[9−11] In recent years, various wet-chemistry and/or pyrolysis-based synthetic approaches have been devised for the production of SACs.[12−14] However, these processes are conducted at high temperatures in reducing gas atmospheres for extended periods, which can cause agglomeration of single atoms and the subsequent degradation of catalytic performance. To enhance the thermal stability of single atoms, support materials can be functionalized with preferential binding sites that strongly trap the guest metal atoms and restrict their migration even at elevated temperatures. N-doped carbon frameworks are an example of such functionalized supports that have been found to stabilize single atoms.[2,15,16] Other methods, such as directly emitting metal atoms from bulk metals onto carbon supports or utilizing ligand-mediated methods, have been explored to generate single atoms.[17−21] Although these strategies are effective for obtaining stable SACs, the preparation of SACs under ambient-air conditions through a momentary process remains a significant challenge in achieving cost-effective and large-scale production for commercialization.

More recently, host-material self-heating (HMH) techniques have been suggested to prepare functional nanomaterials in a straightforward manner. In these techniques, the host materials

Received: April 2, 2023
Accepted: September 28, 2023
Published: October 6, 2023

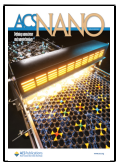

https://doi.org/10.1021/acsnano.3c02968
ACS Nano 2023, 17, 23347−23358

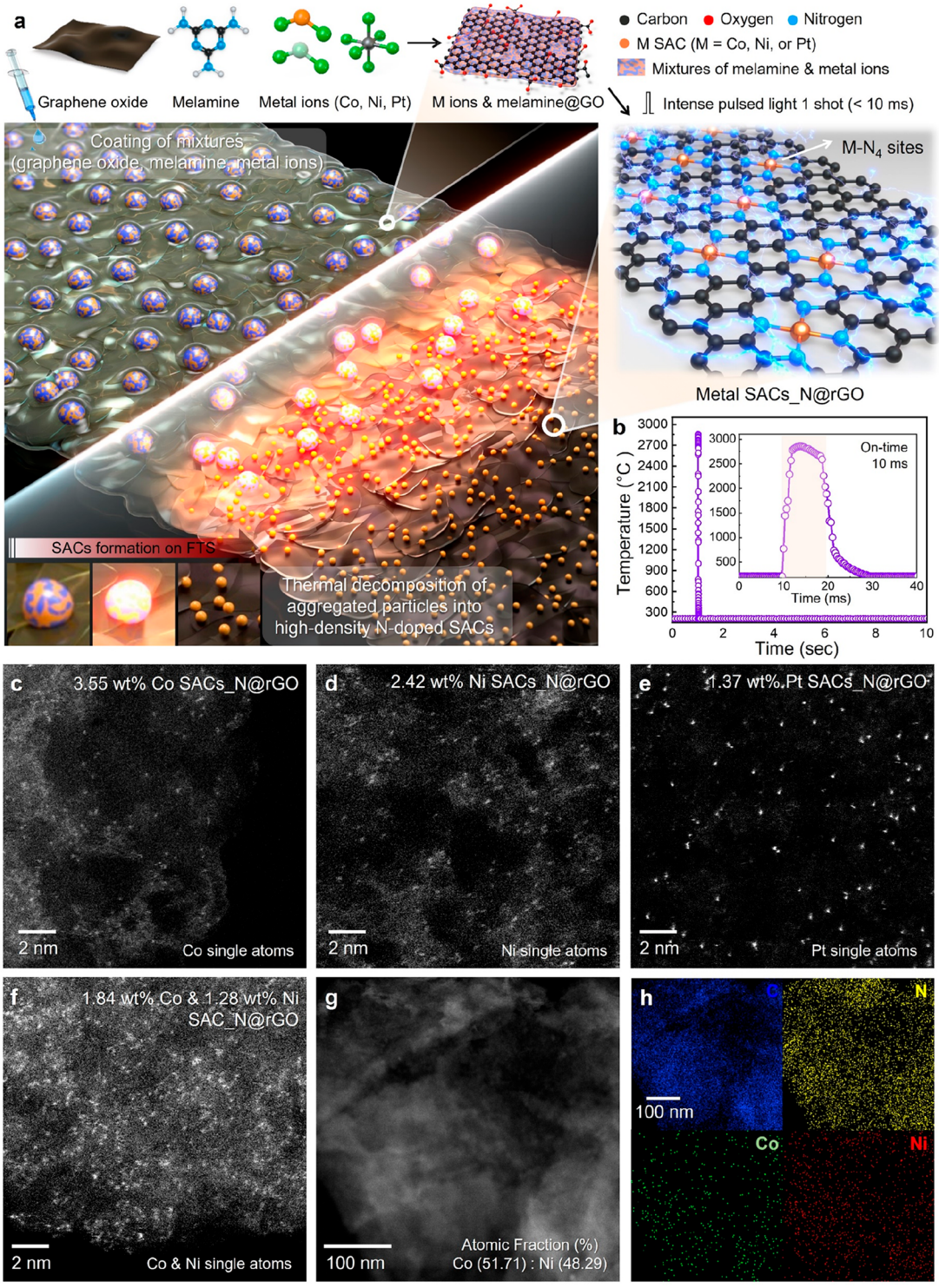

Figure 1. (a) Schematic illustration of the overall flash-thermal shock process for ambient-air synthesis of M SACs_N@rGO. (b) A temperature−time curve of Mel@GO recorded at a constant applied voltage of 450 V for flash light energy density of 10.7 J cm^{-2}. High-angle annular dark-field scanning transmission microscopy images of (c) Co SACs_N@rGO, (d) Ni SACs_N@rGO, (e) Pt SACs_N@rGO, and (f) Co and Ni SACs_N@rGO. (g) STEM and (h) EDS mapping images of Co and Ni SACs_N@rGO.

convert various different sources of energy into heat, whereby their material properties play a key role in the heat generation process. One of the most representative HMH approaches is Joule heating, which converts electrical energy into heat, the efficiency of which depends on the input power and the resistance of the material. Joule heating is generally implemented by carbon nanofibers as a substrate (i.e., host materials) on which guest nanomaterials can be stabilized in the forms of single atoms and/or high entropy alloy nanoparticles by high-temperature thermal shock (over 2000 K within 1 s).[22,23] Despite its advantages to prepare advanced catalysts, the Joule-heating-based self-heating method could be limited to conductive materials and needs a vacuum chamber system with electrode contacts on host materials. As an

https://doi.org/10.1021/acsnano.3c02968
ACS Nano 2023, 17, 23347−23358

alternative, photothermal conversion processes offer an approach for momentary heating. In these processes, the host materials interact with incident phonons, generating photoexcieted electrons. As these electrons collide with the lattice atoms in the host material, their energy is converted into heat-carrying phonons.[24,25] Photothermal conversion can readily induce momentary heating in host materials without needing physical contacts, making it a robust and broadly applicable technique, particularly for the designed synthesis of SACs in ambient-air conditions.

Herein, we propose an ambient-air and noncontact synthetic strategy for producing a series of SACs, including Co, Ni, Pt, and Co−Ni dual component, stabilized on graphene-based substrates via a flash-thermal shock (FTS) lamping process to induce the photothermal effect. A single FTS process, with a duration of less than 10 ms and ramping/cooling rates of approximately 10^5 K/s, enables momentary soaring-temperature annealing (>2850 °C), resulting in simultaneous reduction and N-doping of the graphene oxide (N@rGO) substrate. High-density active N-doping sites formed on the surface of the substrate facilitates anchoring and stabilization of the SACs in high capacities. Uniform atomic distribution of SACs on N@rGO was confirmed by X-ray absorption fine structure (XAFS) and high-angle annular dark-field scanning transmission electron microscopy (HAADF-STEM) analyses. In addition, theoretical simulations were performed to explore the explicit role played by the N-doping sites for the stabilization of SACs. Finally, we demonstrated the utility of SACs-stabilized N@rGO in achieving bifunctional catalytic performances for applications in chemiresistive gas sensing and electrocatalytic oxygen reduction reactions.

RESULTS AND DISCUSSION

FTS Synthesis and Characterization of Single-Atoms-Stabilized N-Doped Graphene. Figure 1a illustrates procedures for ambient-air synthesis of SACs-stabilized N@rGO (SACs_N@rGO) by an intense pulse light (IPL)-induced FTS lamping. First, melamine and metal ion precursors (Co, Ni, and Pt), which are used for N-doping and SACs sources, respectively, are completely dissolved in an aqueous GO dispersion. We have chosen the most widely used catalytic atoms, namely, Co, Ni, and Pt, to demonstrate the potential feasibility of our concepts. Melamine is readily self-assembled on the surface of GO, owing to the large zeta potential difference between GO (−22.48 mV) and melamine (−1.32 mV; Figure S1). Then, the mixture is drop-coated on glass substrates, followed by controlled irradiation of the dried GO-based mixture with a single flash of light from a xenon (Xe) lamp. The irradiated GO experiences a considerable temperature rise due to photothermal conversion.[26,27] Given that the bandgap of GO is distributed from 1.0 to 3.0 eV on the degree of reduction, the wide-range white light from the Xe flash lamp is more suitable for the optical reduction of GO rather than monochromatic light sources such as lasers.[28−30] We found that, with a single flash of light having an energy density of 10.7 J cm^{-2}, the exposed GO mixture underwent a rapid (10 ms) increase in temperature up to 2850 °C. This led to the reduction of GO (rGO), N-doping of the reduced GO (N@rGO), and the homogeneous stabilization of SACs on N-doped sites of N@rGO under ambient-air conditions (Figure 1b and Figure S2). Note that a single flashed light can evenly irradiate a relatively large area (15 cm length × 7.5 cm width), indicating that this method inherently supports high-throughput mass production in industrial applications simply by scaling up the size and number of the lamp (Figures S3 and S4).[31]

Prior to the FTS process on metal ion precursors and melamine-loaded GO (M precursor/Mel@GO, where M = Co, Ni, and Pt), aggregated Co, Ni, and Pt nanoclusters could be observed in the Co precursor/Mel@GO, Ni precursor/Mel@GO, and Pt precursor/Mel@GO, respectively (Figure S5). After the FTS process, the high-angle annular dark-field (HAADF) scanning transmission electron microscopy (STEM) images confirmed the mostly fine distribution of Co, Ni, and Pt SACs on the N@rGO scaffold (Figure 1c−e and Figure S6). Notably, in comparison, the metal atoms tended to aggregate upon FTS without the involvement of melamine, suggesting that the melamine-induced N-doping sites play pivotal roles in stabilizing SACs (Figure S7).[32,33,23] This indicates that while FTS can increase the number of defects on the GO substrate and increase the number of metal binding sites, N doping is essential for reliably stabilizing the SACs. It should be noted that the loading amount of melamine also plays a pivotal role in controlling the extent of N doping, the stabilization level of the metal catalyst, and formation of SACs (Figures S8 and S9). Interestingly, the introduction of FTS on Mel@GO mixtures cofunctionalized with both Co and Ni precursors led to successful synthesis of Co and Ni singly distributed SACs_N@rGO, showing the facile extensibility of the FTS-triggered momentary annealing process beyond the single component system (Figure 1f). The STEM and energy-dispersive X-ray spectroscopy (EDS) overlay mapping images confirmed the fine atomic distribution of Co and Ni SACs throughout the N@rGO (Figure 1g,h). Inductively coupled plasma optical emission spectroscopy (ICP-OES) analysis further confirmed the presences of about 3.6 wt % of Co and 2.4 wt % of Ni on Co SACs_N@rGO and Ni SACs_N@rGO, respectively (see details in Table S1).

Temperature Profiles Using IR Sensor System. We measured the temperature−time profile of Mel@GO at a constant applied voltage of 450 V for flash light energy densities of 1.3, 3.7, 5.4, 7.2, and 10.7 J cm^{-2}, corresponding to pulse-on times of 1, 3, 5, 7, and 10 ms, respectively (see detailed information in Figures S10−S13). The obtained temperature−time curve for the main flash light condition of 10 ms was corrected by referring to the trends from both the 1500 sensor in the range from 200 to 1500 °C and the 3000 sensor in the range from 1500 to 3000 °C (Figure 1c and Figure S13f). Note that 1500 sensor and 3000 sensor could reliably detect temperatures up to 1500 and 3000 °C, respectively. Upon FTS, the surface temperature of the sample reached over 2500 °C within 3 ms. In the following 7 ms, the temperature was held at above 2500 °C with a peak temperature of about 2850 °C. Altogether, the overall on-time was 10 ms. Once the light source was turned off, a sharp decrease in temperature was observed within 6 ms down to the minimum measurable temperature (baseline) of 200 °C, which translates to ultrafast ramping/cooling rates of 7.6×10^5 and 2.7×10^5 K s^{-1}, respectively. As the light energy density increased, the maximum temperature values increased; for instance, the temperature was saturated at around 2850 °C at an energy density of 10 J cm^{-2} (Figure S14). We further investigated the optimal thickness of Mel@GO samples (range of 10−20 μm) that would maximize the FTS-induced temperature with good uniformity, which we set as the standard experimental conditions (Figure S15).

https://doi.org/10.1021/acsnano.3c02968
ACS Nano 2023, 17, 23347−23358

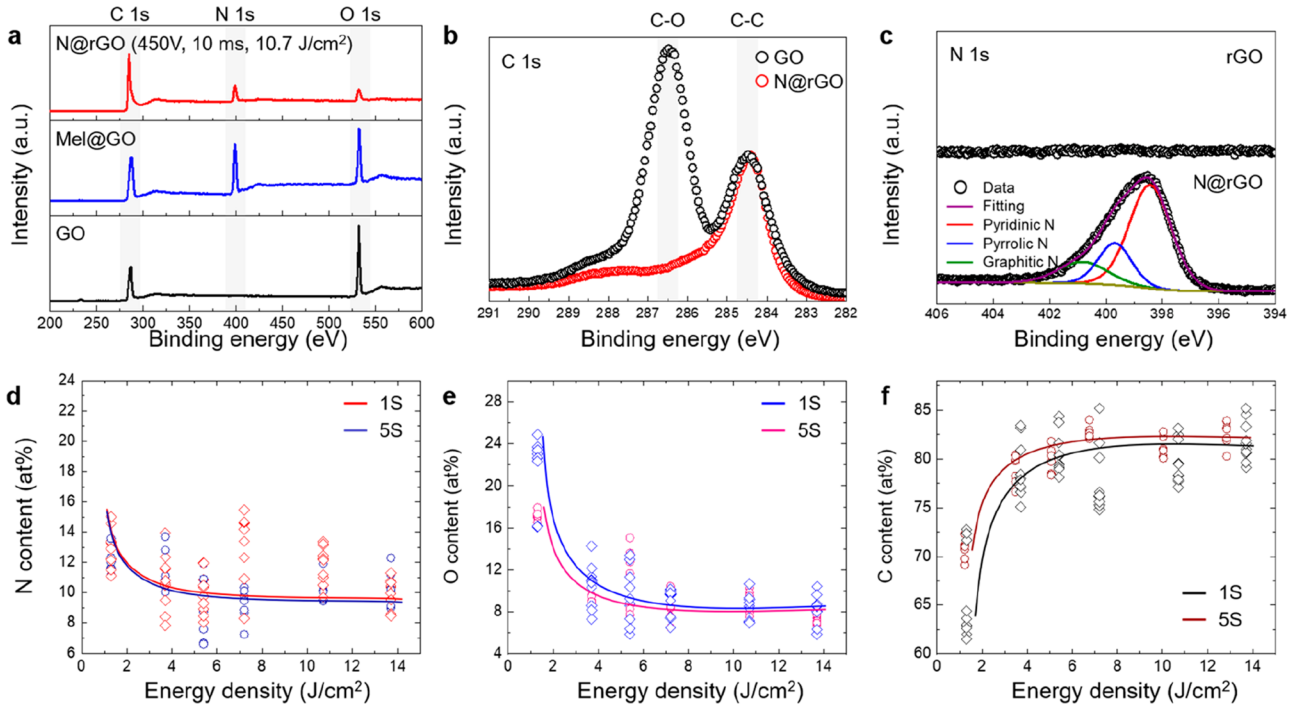

Figure 2. (a) XPS survey scan spectra of GO, Mel@GO, and N@rGO obtained at a light irradiation of 10.7 J cm^{-2} from the IPL. (b) High-resolution C 1s spectra of GO and N@rGO. (c) High-resolution N 1s spectra of GO (upper, without melamine) and N@rGO (lower, with melamine). Atomic percent of (d) N content, (e) O content, and (f) C content from N@rGO depending on IPL energy densities in the range from 1.3 to 13.7 J cm^{-2} and the number of shots (one or five shots).

Analysis of the Reduction and N-Doping on Graphene. The uniformity of N-doping by the FTS process was verified in STEM and EDS mapping images (Figure 1g,h). X-ray photoelectron spectroscopy (XPS) survey spectra were investigated using GO, Mel@GO, and N@rGO at a light irradiation of 10.7 J cm^{-2} (Figure 2a). In the N@rGO sample after the FTS process, O content dramatically decreased while N signals started to appear, demonstrating simultaneous reduction of GO to rGO and N-doping in the rGO lattice.

To examine chemical states and compositions before and after the FTS, high-resolution C 1s and N 1s spectra of GO, pristine melamine, and N@rGO were obtained and compared (Figure 2b,c and Figures S16 and S17). From the C 1s spectra in Figure 2b, C−O related bonds of N@rGO reduced substantially while C−C bonds remained, supporting the fact that GO was reduced to rGO during the FTS process.[34,35] For the N 1s spectra in Figure 2c, the peak intensities related to C−N bonds of N@rGO at 398.4, 399.7, and 400.9 eV, corresponding to pyridinic N (red), pyrrolic N (blue), and graphitic N (green), respectively, were increased.[36−38] The strengthening of these modes indicates that N atoms are located within the 2D lattice of graphene.

Next, we further analyzed the XPS data to study the degree of N-doping and reduction that could be manipulated by changing the IPL energy densities in the range from 1.3 to 13.7 J cm^{-2} and the number of shots from one to five shots (Figure 2d,e). Specifically, we calculated the relative contents of N, O, and C in N@rGO by measurement of the signals from the N 1s, O 1s, and C 1s regions. The N content of ∼13 atom % was acquired at a relatively weak energy density (1.3 J cm^{-2}), but it slightly decreased down to ∼10 atom % in higher energy densities (1.3−13.7 J cm^{-2}; Figure 2d). As for the O and C contents, however, a difference was observed in the number of shots, especially at a weak energy density (1.3 J cm^{-2}), leading to enhanced reduction (Figure 2e,f). With energy densities higher than 4.0 J cm^{-2}, the O and C contents became saturated at around 8 and 82 atom %, respectively, regardless of the number of shots and energy densities. Overall, we demonstrated that the degree of reduction and N-doping could be optimized simply by tuning the settings for the IPL experiment. It is noteworthy that reduction of GO even through furnace annealing at 750 °C for 1 h in NH_3 also leads to O residues (3−5 atom %) on the surface of rGO,[39] possibly leading to slight oxidation of the catalyst with GO support. We believe that the oxidation issue can be ruled out by the introduction of high photothermal materials, e.g., carbon black, which do not contain oxygen species.

In most fabrication processes of SACs on N-doped graphene, inert atmospheres are necessary to anneal the sample without damaging it at elevated temperatures for a long time (>1 h; Table S2). This necessitates a costly gas-storage system for inert gases as well as a high energy expenditure for maintaining the high temperature. However, our FTS method can be performed in ambient air with an extremely short burst of irradiation (<10 ms) onto samples, enabling a facile and high-throughput process. In spite of the simplicity of this approach, the concentration of N-doping in GO is comparable to those of the others achieved by conventional (energy- and time-consuming) furnace annealing. We further confirmed that the N@rGO has a high specific surface area (82.56 m^2 g^{-1}) with abundant mesopores (2−50 nm) based on rapid interplanar volume expansion due to the evolution of gaseous species during FTS (Figure S18).

Analysis of the Single-Atom Bond Structure. During the momentary FTS-heating process, we expect sequential steps of reduction, N-doping, and anchoring of single atoms to

https://doi.org/10.1021/acsnano.3c02968
ACS Nano 2023, 17, 23347−23358

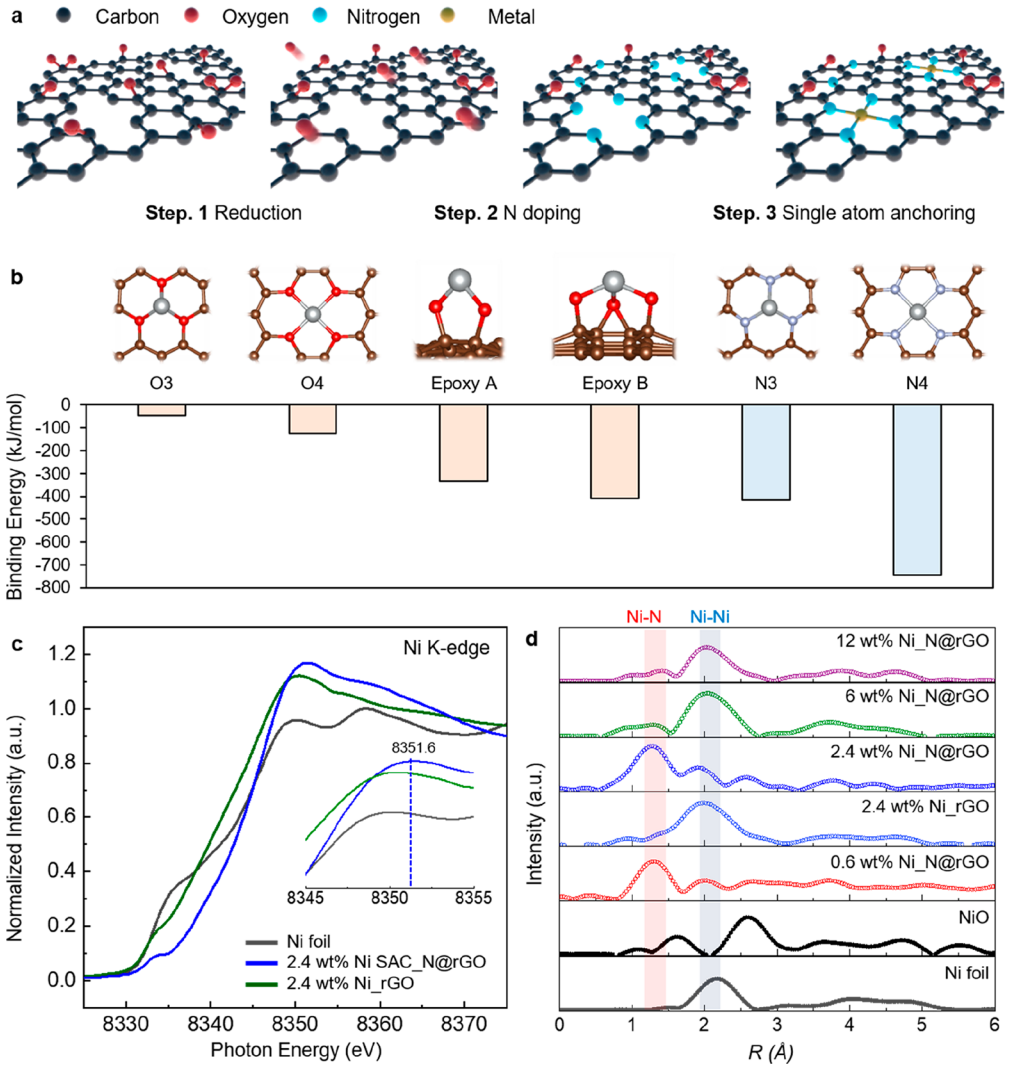

Figure 3. (a) Schematic illustrations of the synthesis of SACs_N@rGO in three steps; (i) reduction, (ii) N doping, and (iii) single atom anchoring. (b) Binding energies of a single Ni atom on the defects sites of rGO provided by N-doping sites and oxygen functional groups. (c) Ni K-edge X-ray absorption near edge structure spectra of Ni foil, 2.4 wt % Ni_rGO, and 2.4 wt % Ni SACs_N@rGO. (d) Fourier transform radial distribution function of the Ni K-edge k^3-weighted EXAFS spectra of Ni foil, NiO powder, Ni_rGO, and four Ni_N@rGO samples with different Ni contents (0.6, 2.4, 6.0, and 12.0 wt %).

take place for the preparation of M SACs_N@rGO (Figure 3a). In our previous study, we systematically demonstrated that the FTS approach enabled the reduction of GO within 1 ms and further achieved heteroatom doping above 1400 °C in the millisecond-scale and ambient-air treatment.[35] Thus, it seems reasonable that the reduction and doping process would be finished step by step within 3 ms from Figure 1b, which is consistent with the result showing that N, O, and C contents became saturated above 3.7 J cm^{-2} (Figure 2e−g). The transient atomic structure formed during the FTS process could provide energetically favorable $M-N_4$ bonding sites for stable single-atom anchoring. It was also reported that N sites play an important role in anchoring SACs at high temperature above 600 °C due to prevaporations of oxygen atoms.[40] The high-resolution XPS analysis conducted on Ni SAC_N@rGO in the vicinity of the O 1s and Ni 2p peaks confirmed the creation of Ni in a SAC configuration, with no evidence of oxidized phase formation (Figure S19).

To further elucidate the exact mechanism behind the facile formation of SACs on N@rGO, especially for Ni SACs, density functional theory (DFT) calculations were performed. In detail, we proposed several different point vacancy defect scenarios for rGO with one or two missing atoms before and after N doping (Figure S20). Such point vacancy defect scenarios were primarily targeted, as they correspond to the pyridinic defect sites, which were abundantly found in the experimental data. Here, defect scenarios of rGO prior to N doping undergo C−C bond formation upon geometry optimization due to the presence of dangling bonds. This unusual behavior hints at the high instability of these sites, which in reality would be extremely prone to oxidation or contamination. The same defect scenarios after N doping show no significant structural transformation, as no dangling bonds with unpaired electrons would be present due to the influence of the doped nitrogen atoms. As such, N-doping of rGO helps retain the energetic defect sites at which SACs forms. Next, binding energies of the Ni atom at the defect site of N-doped rGO were calculated, and the results are shown in Figure 3b. Here, the highest binding energy for the Ni atom in SACs formation is provided by the N_4 case (i.e., Ni bonded to four

https://doi.org/10.1021/acsnano.3c02968
ACS Nano 2023, 17, 23347−23358

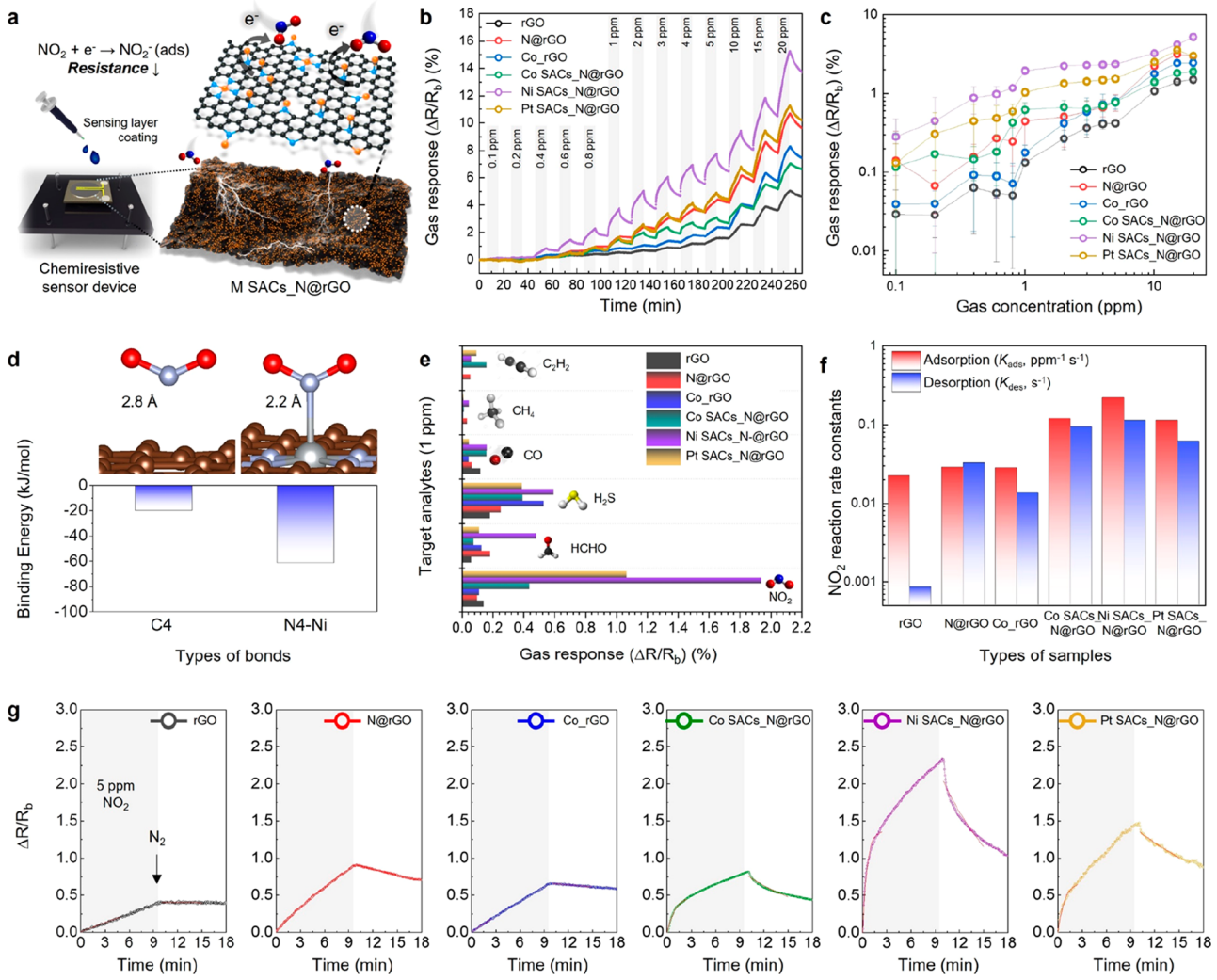

Figure 4. (a) Schematic illustrations of the sensor device. (b,c) Dynamic gas sensing performance of rGO, N@rGO, Co-rGO, and M SACs_N@rGO (M = Co, Ni, and Pt) toward 0.1−20 ppm of NO_2 gas. (d) Calculated adsorption energies of NO_2 at C_4 and N_4−Ni sites (brown, C; gray, Ni; blue, N; red, O). (e) Selective gas sensing properties. (f) Rate constants for the NO_2 reactions. (g) Response and recovery fitting curves and raw response and recovery curves for NO_2 sensing.

adjacent nitrogen atoms), whereby the binding energy reaches −743.7 kJ/mol. In the N_3 case, a binding energy of −418.4 kJ/mol is observed. For reference, the binding energy of Ni onto the oxygen-containing surface moieties is calculated to be −335.8 and −409.6 kJ/mol, which is far less in magnitude compared to the Ni−N_4 binding energy. These results demonstrate that adsorption of Ni atoms on rGO for SACs formation is dramatically promoted by N-doping of the material, which leads to the creation of pyridinic defect sites with notably higher metal binding energies.

As experimental evidence for the successful formation of SACs, we conducted X-ray absorption spectroscopy (XAS) analyses, which include X-ray absorption near edge structure (XANES) and extended absorption fine structure (EXAFS) measurements. In the Ni K-edge normalized XANES spectrum as shown in Figure 3c, the near-edge absorption energy of Ni SACs_N@rGO was measured to be higher (8351.6 eV) than that of metallic Ni measured from the reference Ni foil, which implies that the Ni atoms are in oxidized states with $Ni^{\delta+}$ valence ($\delta < 2$). This is attributed to the Ni−N_4 bonds in Ni SACs_N@rGO, where the highly electronegative N atoms draw the valence electrons from the Ni atom to induce higher oxidation states. The Ni K-edge spectra in the Fourier transform EXAFS analysis more evidently demonstrate the formation of well-dispersed Ni SACs in Ni SACs_N@rGO samples (Figure 3d). Herein, we investigated the effects of the Ni content and N-doping sites on the uniformity of Ni SACs. In this regard, we prepared N@rGO loaded with four different Ni contents (0.6, 2.4, 6.0, and 12.0 wt %) and, as a reference, rGO prepared with 2.4 wt % loading of Ni. In EXAFS spectra of the k^3-weighted Ni K-edge, 0.6 wt % Ni SACs_N@rGO and 2.4 wt % Ni SACs_N@rGO samples showed distinct peaks at about 1.3 Å, which are assigned to Ni−N bonds. Meanwhile, 6.0 wt % Ni_N@rGO, 12.0 wt % Ni_N@rGO, and 2.4 wt % Ni_rGO samples mainly exhibited peaks at about 2.1 Å associated with Ni−Ni bonds, with a negligible contribution from the Ni−N peak. The fitted EXAFS spectra for the first shell (Ni−N and Ni−Ni) exhibit clues to the formation of Ni−N bonding in Ni SACs_N@rGO (Figure S21). The calculated coordination numbers (CN) of Ni−Ni and Ni−N in Ni_N@rGO are listed in Table S3. The CN of Ni−N increased from 0.60, 2.16, 3.92, to 3.98 as the Ni content decreased from 12.0, 6.0, 2.4, and 0.6 wt %, respectively. The CNs of Ni−Ni were 1.08 and 3.60 for 2.4 wt % Ni_N@rGO and 6 wt % Ni_N@

https://doi.org/10.1021/acsnano.3c02968
ACS Nano 2023, 17, 23347−23358

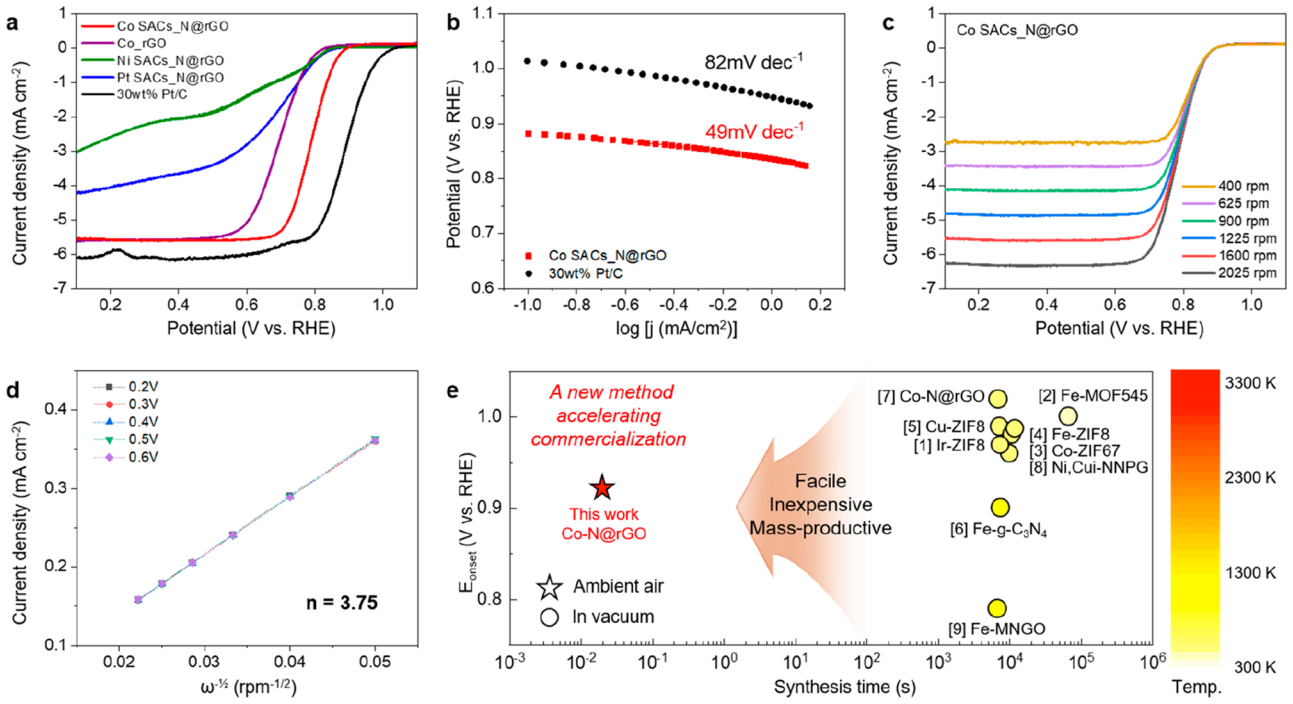

Figure 5. Electrochemical measurements of Co SACs_N@rGO: (a) Linear sweep voltammetry (LSV) curves of the ORR for the Co SACs_N@rGO, Co_rGO, Ni SACs_N@rGO, Pt SACs_N@rGO, and commercial 30 wt % Pt/C in an O_2-saturated 0.1 M KOH solution at a rotation speed of 1600 rpm and a scan rate of 5 mV s^{-1}. (b) Tafel plots of Co SACs_N@rGO and commercial 30 wt % Pt/C. (c) LSV curves of the ORR for the Co SACs_N@rGO in an O_2-saturated 0.1 M KOH solution at different rotation speed of 400 to 2025 rpm and a scan rate of 5 mV s^{-1}. (d) The corresponding K−L plots of J^{-1} versus $\omega^{-1/2}$ of Co SACs_N@rGO in the different potential ranging from 0.20 to 0.60 V. (e) Summary of recent results based on single atoms in N-doped carbon supports toward ORR performance (E_{onset}) and their synthesis times through our method and other techniques (Table S5). The color in the figure indicates synthesis temperature on the right colormap. NNPG and MNGO stand for N-doped nanoporous graphene and mesoporous nitrogen-doped GO, respectively.

rGO, respectively. The fit for the first shell gives a distance (R) of about 2.46−2.50 Å and 1.81−1.85 Å for Ni−Ni and Ni−N, respectively. While further optimization processes are required to obtain higher density and more uniform Ni SAC formation without the formation of any nanoclusters, this work demonstrates the strong potential for synthesizing SACs in a simple process under ambient air conditions. Overall, the XAS analyses indicate that the melamine-induced N-doping and Ni loading amount are important control factors for the successful synthesis of SACs. It is worth pointing out that state-of-the art synthetic methods for SACs on N-doped carbon supports were all performed in a vacuum system, while our work was carried out in ambient air. Even so, the loading amount of metal single atoms and the level of N-doping were comparable or even higher compared to the other cases (Tables S2, S4, S5).

Chemiresistive Gas Sensing Application. The rationally designed single-atom nanostructure of SACs_N@rGO is expected to provide several benefits for a variety of practical applications, one of which could be found in chemiresistive gas sensing. In particular, defect-rich N@rGO would readily interact with gas molecules (e.g., NO_2) through surface chemical reactions, while metal single atoms would serve as highly active catalysts for enhancing the sensing performance overall. As a practical demonstration, we fabricated gas sensors based on the active materials by coating them onto alumina substrates patterned with Au electrodes (Figure 4a). For a comparative evaluation, we prepared six different sensing layers including rGO, N@rGO, Co-rGO, Co SACs_N@rGO, Ni SACs_N@rGO, and Pt SACs_N@rGO and tested their respective gas sensing characteristics upon exposure to 0.1−20 ppm of NO_2 gas (Figure 4b,c).

It is known that NO_2, a common industrial byproduct gas that is toxic to human health and must be closely monitored in the environment, can either physisorb on the rGO surface or chemically react with oxygen species, which would attract the electrons in the rGO-based layers toward the gas molecules and decrease the resistance of the rGO-based materials (eqs 1 and 2).[35,41]

$$NO_2(gas) + e^- \rightarrow NO_{2(ads)}^- \quad (1)$$

$$2NO_2(gas) + O_2(gas) + 2e^- \rightarrow 2NO_{3(ads)}^- \quad (2)$$

The performance of the sensor was quantified using the sensitivity ($\Delta R/R_b$ [%], where ΔR and R_b denote resistance variation in the presence of the target gas and baseline resistance under ambient conditions without the target gas, respectively). Notably, Ni SACs_N@rGO exhibited on average 9.6-fold improved NO_2 sensing response toward 0.1 ppm of NO_2 compared to pristine rGO. In particular, we found that the optimal sensing properties in terms of the response value were achieved with 2.4 wt % of Ni content (Figure S22). DFT calculations demonstrated that NO_2 has about 3.1-fold stronger binding energy (− 61.19 kJ mol^{-1}) with the $Ni-N_4$ binding sites compared to that (−19.93 kJ mol^{-1}) with the C_4 binding sites of pristine rGO, which explains the improvement in the response for the case involving Ni SACs (Figure 4d). We investigated the selective gas sensing characteristics of SACs-based sensors toward NO_2, against interfering gas species including formaldehyde (HCHO), hydrogen sulfide (H_2S),

https://doi.org/10.1021/acsnano.3c02968
ACS Nano 2023, 17, 23347−23358

carbon monoxide (CO), methane (CH_4), and ethylene (C_2H_2; Figure 4e). As a result, rGO and N@rGO showed poor selectivity toward NO_2 as it showed similar responses ($\Delta R/R_b$ = 0.1−0.2%) toward NO_2, HCHO, H_2S, and CO analytes. Ni SACs_N@rGO and Pt SACs_N@rGO showed highly selective responses toward NO_2, which is likely to be attributed to the enlarged chemisorption of NO_2 on the metal (Ni or Pt)-stabilized N-rGO.[42,43]

We further conducted reversible sensing tests using rGO, N@rGO, and Ni SACs_N@rGO to investigate the effects of N-doping and SACs on the overall reliability of the gas sensors (Figure S23). The pristine rGO sensor showed continuous downward drifts in gas response because of the incomplete recovery, indicating that the desorption of nitrious adsorbents was not facilitated with rGO alone. Meanwhile, N@rGO and Ni SACs_N@rGO sensors showed enhanced reversibility, indicating the role of N doping, improving the electrical conductivity, which accompanies facile electron transfer. We further investigated the NO_2 reaction rate constants during the adsorption and desorption of NO_2 analytes (Figure 4f,g). As a result, N@rGO showed about 1.29- and 37.73-fold improved adsorption and desorption rate constants over pristine rGO. Functionalization with SACs (Co, Ni, or Pt) on N@rGO further improved the reaction kinetics. In particular, Ni SACs_N@rGO exhibited about 7.65- and 3.48-fold enhanced adsorption and desorption rate constants, respectively, over N@rGO. Ex situ XPS analyses confirmed that the Ni SACs hold advantages in accelerating the recovery process by effectively eliminating adsorbed nitrates (NO_3^-; Figure S24). Altogether, the SACs that are rationally engineered through our strategy exhibited good sensing characteristics in terms of response, selectivity, reversibility, and reaction rates.

Electrocatalytic Application. The SACs_N@rGO can also facilitate electrocatalytic oxygen reduction reaction (ORR), which is an essential component of various fuel cell systems. To this end, the electrocatalytic properties of SACs_N@rGO were compared on alkaline media under a three electrode system (Figure S25). Specifically, the ORR electrocatalytic activities of the Co SACs_N@rGO, Co_rGO, Ni SACs_N@rGO, Pt SACs_N@rGO, and commercial 30 wt % Pt/C were examined in O_2-purged 0.1 M KOH by using rotating disk electrode measurements (Figure S26). The linear sweep voltammogram (LSV) curves reveal that the Co SACs_N@rGO features a higher ORR activity in view of the onset (E_{onset}) and half-wave ($E_{1/2}$) potentials over the other FTS samples (Figure 5a). Co_rGO without N doping features a much lower ORR performance than Co SACs_N@rGO. These results indicate that the Co−N_4 active sites formed during the FTS method are critical for boosting the ORR activity over Co nanoparticles. Notably, the $E_{1/2}$ of Co SACs_N@rGO (0.80 V) was more positive than that of Pt SACs_N@rGO (0.67 V) by a difference of 130 mV. This can be attributed to the fact that a decrease in the Pt particle size to the atomic scale could lead to an excessive increase in the oxygen binding energy, resulting in reduced ORR activity.[44] In addition, Co SACs_N@rGO obtained on various IPL shot numbers and Co contents also show similar E_{onset} values (~0.92 V; Figure S27). Also, as shown in Figure 5b, the Tafel slope of Co SACs_N@rGO (49 mV dec^{-1}) is lower than that of the commercial Pt/C catalyst (82 mV dec^{-1}), representing faster kinetics. Moreover, LSV tests under various rotation speeds (400−2025 rpm) were conducted to probe the catalytic kinetics (Figure 5c). The corresponding Koutecky−Levich (K−L) plots at different potentials present good linearity with similar slopes, which indicates first-order reaction kinetics with respect to the oxygen concentration. On the basis of the K−L equation, an average electron transfer number (n) of 3.75 was yielded for Co SACs_N@rGO (Figure 5d). This value, which is very close to 4, indicates that the oxygen reduction processes on the Co single atomic sites proceed through the four-electron pathway of direct O_2 reduction to OH^- under alkaline media with reasonable selectivity, achieving high energy efficiency with minimal side reactions (H_2O_2 formation). The stability of Co SAC_N@rGO was evaluated through CV measurements in O_2-saturated 0.1 M KOH solution. Importantly, even after 10 000 repeated CV cycles (Figure S28), a negligible decay in $E_{1/2}$ (~8.7 mV) was observed, indicating the high stability of the SAC catalyst on graphene compared to commercial Pt/C catalysts ($E_{1/2}$ shift = 14.7 mV). Comparing the change in the Tafel slope derived from the LSV curves before and after CV cycle tests, the Tafel slope of commercial Pt/C catalysts changed from 82 mV dec^{-1} to 98 mV dec^{-1}, while for Co SACs_N@rGO, the Tafel slope exhibited a change from 72 mV dec^{-1} to 81 mV dec^{-1}. The slight changes in the $E_{1/2}$ shift and Tafel slope before and after the durability test show good ORR electrochemical stability of SACs.

To further highlight electrochemical properties of M SACs_N@rGO (M = Co, Ni, Fe), we carried out LSV tests (at 1600 rpm) for the oxygen evolution reaction (OER) and hydrogen evolution reaction (HER), respectively, under alkaline media (Figure S29). In the OER performance, Ni SACs_N@rGO was confirmed to have the lowest onset potential, but Co SACs_N@rGO showed high current density due to low electrical resistance. Similarly, in the HER performance, Co SACs_N@rGO showed the lowest overpotential, confirming that Co−N_4 sites provide the most effective active characteristic. Ultimately, these results demonstrate the versatility of our method for synthesizing SACs with high catalytic activity as well as catalytic selectivity toward specific electrochemical reactions simply by changing the type of metal being used for SAC fabrication (Tables S4 and S5). Last, it should be noteworthy that besides decreasing loading of noble metals in a cost-effective way, a synthetic approach such as FTS could be an alternative solution to accelerating commercialization of various catalytic applications (Figure 5e).

CONCLUSION

This study presents the approach for the site-specific anchoring of single atoms (Pt, Co, Ni, and Co−Ni) on the N-doped graphene supports using the flash-thermal shock (FTS) lamping. The ambient-air, noncontact, and robust synthetic strategy allows for extremely high temperature annealing (>2850 °C) of graphene oxide (GO), with melamine and metal salts as N-doping and SACs sources, respectively, within 10 ms to enable the sequential and synchronous reduction of GO, N-doping (>10 at%), and stabilization of single atoms on graphene-based supports. The resulting SACs_N@rGO samples were systematically characterized by various advanced experimental techniques, including X-ray absorption fine structure (XAFS) and high-angle annular dark-field scanning transmission electron microscopy (HAADF-STEM) analyses, which were supported by a theoretical framework based on DFT calculations, to highlight the key role played by N-doping sites for stabilization of SACs. The bifunctional performances of SACs_N@rGO were verified in chemiresistive gas sensing

https://doi.org/10.1021/acsnano.3c02968
ACS Nano 2023, 17, 23347−23358

and electrocatalytic activities, demonstrating their high surface activities and potential ultization in a variety of applications. Notably, Ni SACs_N@rGO exhibited good NO_2 gas sensing characteristics, and Co SACs_N@rGO showed reasonable ORR performances (i.e., an average electron transfer number (n) of 3.75 and half-wave potential ($E_{1/2}$) of ~0.80 V) that are comparable to those of SACs samples obtained by conventional furnace annealing processes in vacuum systems. Most importantly, our ultrafast FTS process provides several key advantages for practical utilization of SACs on an industrial scale without vacuum facilities, suggesting a method to prepare highly active catalytic materials with practical implications.

EXPERIMENTAL SECTION

M-Mel@GO Coating on Substrates. Melamine, metal salts, and GO dispersed DI solution (4 mg mL^{-1}) were purchased from Sigma-Aldrich (St. Louis, USA). All chemicals were used without further purification. For N-doping of GO, 6 mg of melamine in 2 mL ethanol was mixed with 2 mL of GO dispersed DI solution, then ultrasonicated for 2 h. To obtain SACs_N@rGO, an appropriate amount of 0.03 M metal precursor solution was added to the as-prepared mixture of melamine and GO solution. Then, 100 μL of the final mixture was drop-coated on the glass substrate with a micropipette several times and dried in ambient air for an hour prior to the FTS process.

Materials Characterization. The TEM images were analyzed by transmission electron microscopy (TEM; Tecnai G2 S-Twin, FEI). The high-angle annular dark-field scanning TEM (HADDF-STEM) and energy dispersive X-ray spectroscopy (EDS) analysis were carried out by aberration-corrected TEM (JEMARM200F, JEOL) and double-aberration-corrected TEM (Titan Themis-3 Double Cs & Mono, FEI; Titan cubed G2 60−300) equipped with Chemi-STEM and X-FEG system. Thermal stability was investigated by thermal gravimetric analysis (TGA, Labsys Evo, Setaram). The chemical binding states were confirmed by X-ray photoelectron spectroscopy (XPS Sigma Probe, Thermo VG Scientific) with Al Kα irradiation (1486.6 eV). XAS measurements were performed on beamline 10C at the Pohang Accelerator Laboratory (PAL, Pohang, South Korea). All XAS spectra were acquired at room temperature in fluorescence mode using a double-crystal Si(111) monochromator. Analyses of both the near edge (in energy scale) and extended range (in R space) XAS spectra were performed using Athena software and fitting was conducted using Artemis software. To identify the Brunauer−Emmett−Teller (BET) surface area and pore size distribution, we collected N_2 adsorption/desorption isotherms for interpretation and analysis (Tristar 3020, Micromeritics) at 77 K.

Reduction and N-Doping of GO and SACs Formation by IPL Irradiation. Intense pulsed light (IPL) with a xenon flash lamp (PLT, Photocura) was introduced to realize reduction and simultaneous N-doping, finally leading to the formation of SACs on the surface of N@rGO sheets in ambient air. The light generated by the xenon lamps features broad-spectrum wavelengths ranging from about 300 to 1000 nm. Output light energy from the lamp can be adjusted by tuning the applied voltage, stored capacitance in capacitors, pulse number, pulse on/off time, and sample distance from the lamp. Normally, it is known that the intensity of output at wavelengths longer than 700 nm becomes enhanced when the total light energy increases by various operation factors. First, the glass substrates coated with Mel@GO sheets and M-Mel@GO were placed at a 4 cm distance from the lamp. Light irradiation was performed with the pulse on-time of 10 ms and a constant applied voltage of 450 V to the lamp to maintain the output light energy as 10.7 J cm^{-2}. A single light pulse generated from a xenon lamp was irradiated onto the Mel@GO sheets and M-Mel@GO [metal ion precursors (M) of Co, Ni, and Pt] coated on the glass substrates for the ambient-air synthesis of N@rGO and SACs_N@rGO. For the uniform FTS-treatment, light irradiation was alternately performed on both sides of the sample. Finally, a series of filtration processes was carried out through the dissolution of melamine in ethanol to remove the residue.

IR Sensor System for Accurate Measurement of Temperature during IPL. For IR sensor systems, different kinds of IR thermometers were introduced to improve the accuracy of the temperature measurement. First, IR information featuring a wavelength of 2.3 μm from samples is detected with an IR thermometer (CTlaser 3MH2, Optris). It should be noted that the baseline of temperature is shown at 200 °C, reflecting the detectable temperature range from 200 °C up to 1500 °C. However, it is often observed that the measured temperature reaches the upper limit (1500 °C) of the IR sensor (CTlaser 3MH2) due to the high photothermal efficiency of GO. Accordingly, other IR thermometers were introduced (thermoMETER CTRatio CTRM-1H1SF100-C3 and CTRM-2H1SF100-C3 from Micro-Epsilon) in order for high temperature measurement above 1500 °C. Both of these IR thermometers are capable of supporting temperature measurement up to 3000 °C by detecting light radiating from the target in the wavelength of 0.8 and 1.5 μm for the model CTRM-1H1SF100-C3 and CTRM-2H1SF100-C3, respectively. Because the wavelength of 0.8 μm belongs to the spectrum of the Xe lamp, with the model CTRM-1H1SF100-C3, the temperature kept being measured as the maximum (3000 °C) due to the noise effect. On the other hand, the CTRM-2H1SF100-C3 with a detectable wavelength of 1.5 μm is able to achieve accurate measurement with insignificant noise coming from the Xe lamp. Experimentally, the temperature values were obtained with the emissivity value of the IR sensor set at unity. Considering the real emissivity of carbon-based materials (i.e., 0.79), emissivity correction renders the temperature upper limit of each IR sensor increase up to about 1630 °C for CTlaser 3MH2 and 3290 °C for CTRM-2H1SF100-C3. For minimization of signal latency below a millisecond, a data acquisition system was established to correct and convert measured analog signals into digital signals. Given that the IR sensors send analogue current output from 4 to 20 mA, an analogue current input module (NI 9203 screw terminal 779516−01, National Instruments) was wire-connected to the IR sensors with a USB compact DAQ chassis (cDAQ-9171 781425−01) for better connection compatibility to a computer. Finally, LabVIEW software was used to control the receiving current signal from the thermometers.

Gas Sensing Characterization. The sensing materials were coated on the Al_2O_3 substrate, patterned with two parallel electrodes (25 and 70 μm of width and separation distance, respectively). Pristine rGO, N@rGO, Co-rGO, Co SACs_N@rGO, Ni SACs_N@rGO, and Pt SACs_N@rGO were used as sensing materials. The sensing characteristics were evaluated by using homemade testing equipment, which is described in detail elsewhere.[35] The resistance of the sensors was measured every 4 s using a data acquisition system (34972A, Agilent) with a 16-channel multiplexer (34902A, Agilent). The measured resistance values were converted into a response by normalizing the change in resistance upon exposure to target gas by the base resistance of the sensor under baseline conditions. Prior to the sensing tests, all of the sensors were stabilized in the baseline atmosphere for 2 h. The gas concentration was controlled as 0.1−20 ppm with a cyclic exposure of the target gas and baseline N_2 for 10 min, respectively. All of the sensing tests were conducted at room temperature. In addition, adsorption (K_{ads}) and desorption (K_{des}) rate constants were calculated by fitting the response vs time graphs of each samples by using eqs 3 and 4:

$$R(t) \text{ for } NO_2 \text{ adsorption} = R_{max} \cdot \frac{C_a K}{1 + C_a K}\left(1 - \exp\left[-\frac{1 + C_g K}{K} \cdot k_{ads} t\right]\right) \quad (3)$$

$$R(t) \text{ for } NO_2 \text{ desorption} = R_0 \exp[-k_{des} t] \quad (4)$$

where R_{max} is the maximum response, R_0 is the response in baseline N_2, C_a is the gas concentration, t is time, and K is an equilibrium constant (K_{ads}/K_{des}). Based on the mass action law of NO_2 adsorption/desorption on rGO-based sensing layers that the amount

https://doi.org/10.1021/acsnano.3c02968
ACS Nano 2023, 17, 23347−23358

of surface-adsorbed gas is proportional to the response, the corresponding reaction rate constants were calculated.[45]

Computational Details. Density functional theory (DFT) analysis was conducted with Vienna *Ab initio* Simulation Program (VASP) software. The projector-augmented wave (PAW) method was used to describe the electron−ion interactions, and the Perdew−Burke−Ernzerhof (PBE) functional was used for the generalized gradient approximation (GGA) of the exchange-correlational energy. A 400 eV kinetic energy cutoff was enforced for all calculations, and a 0.01 eV/Å atomic Hellman-Feynman force threshold was additionally used for the geometry optimization calculations. A 2 × 2 × 1 Monkhorst−Pack k-point grid was used, and 20 Å vacuum layer was introduced in the direction perpendicular to the graphene to limit any sheet-to-sheet interaction. All surface groups for single atom catalyst deposition were modeled on a sufficiently large 6 × 8 supercell of graphene (15 Å × 17 Å) to prevent lateral self-interactions of the surface groups. Binding energies of the single metal ions were computed as follows: $E_{B.E.metal}) = E_{complex} - (E_{func.graphene}) + E_{metalion})$ In cases where the binding energy of the gas molecule was computed, the same convention was applied: $E_{B.E.gas} = E_{complex} - (E_{SACgraphene}) + E_{gasmolecule})$

Electrochemical Half-Cell Tests. All electrochemical measurements were performed using a conventional three-electrode rotating ring disk system using a Wonatech Zive MP1 multichannel potentiostat. For the working electrodes, 4 mg of M SACs_N@rGO samples were mixed with 4 mg of Super P into 80 μL of Nafion solution (5 wt %, Sigma-Aldrich) added to a 1 mL of DI water/isopropyl alcohol (IPA) solution (v/v = 3:1). The catalyst ink-loaded glassy carbon electrode (GCE; geometric area, 0.196 cm^2) was used as a working electrode, and an Ag/AgCl electrode and Pt wire were used as the reference electrode and counter electrode, respectively. For electrochemical three-electrode tests, all SACs_N@rGO catalyst samples were treated with sonication with solvents (DI water and IPA mixed solution). After vigorous mixing with ultrasonication, 14 μL of the homogeneous catalyst ink was transferred onto the GCE (loading amount of catalysts was 2.64 mg cm^{-2}) and dried at 60 °C for the measurements. The dried GCE was then transferred to the rotating disk electrode (RDE) setup, and O_2 saturated 0.1 M KOH aqueous solution was used as the electrolyte for both the ORR and OER measurements. N_2 saturated 0.1 M KOH was used for the HER measurement. All polarization curves were obtained at a scan rate of 5 mV s^{-1} with different rotating speeds under an O_2-gas flow, and the potentials were measured with a Ag/AgCl reference electrode and referred to a reversible hydrogen electrode (RHE) following the Arrhenius eq 5:

$$E_{RHE} = E_{measured} + E^{\circ}_{Ag/AgCl}\,(0.196\,V) + 0.059\,V \times (pH \sim 13)$$
$$= E_{measured} + 0.963\,V \quad (5)$$

The calculation of the apparent electron transfer number (n) for ORR using Koutechy-Levish (K-L) eq 6.[46]

$$\frac{1}{I} = \frac{1}{i_L} + \frac{1}{i_K} = \frac{1}{i_L} + \left(\frac{1}{0.620nFAD^{2/3}\upsilon^{-1/6}C}\right)\omega^{-1/2} \quad (6)$$

where I is the measured current, i_L is the limited current, i_K is the kinetic current, ω is the electrode rotation speed in rpm, F is the Faraday constant (96 485 C mol^{-1}), C is the bulk concentration of dissolved oxygen gas (1.2×10^{-6} mol cm^{-3}), D is the diffusion coefficient of oxygen gas (1.9×10^{-5} cm^2 s^{-1}), and ν is the kinematic viscosity of the electrolyte (0.01 cm^2 s^{-1}).

ASSOCIATED CONTENT

Supporting Information

The Supporting Information is available free of charge at https://pubs.acs.org/doi/10.1021/acsnano.3c02968.

Supplementary notes on IR sensor system for ms-scale temperature measurement; zeta potential values; TG/DSC analysis; optical images of IPL system and spectral information on the xenon flash lamp; TEM/STEM images of metal precursor@Mel@GO. HAADF-STEM images of metal SAC_N@rGO and metal@rGO without melamine; XPS analysis of melamine, GO, N@rGO, and Ni_N@rGO; temperature−time curves using USB connecting and DAQ board connecting; system interface diagram and optical images of IR sensor system; spectral information on Xe flash lamp and temperature transients of the stage and materials with the IR sensors; temperature−time curves of Mel@GO obtained from 1500- and 3000-sensors; peak temperature of Mel@GO at various IPL conditions; cross-sectional SEM images and peak temperature of Mel@GO; BET surface area and pore size distribution of N@rGO; DFT-optimized configurations of the rGO defect sites before/after N-doping; EXAFS spectra and their fits; sensing response of Ni_SACs N@rGO with various Ni content; NO_2 sensing reliability tests; XPS analysis of before and after exposure to NO_2 gas; ORR electrochemical performance of Co_rGO and M SACs_N@rGO; LSV curves of the ORR before and after 10 000 cycles; OER and HER electrochemical performance of M SACs_N@rGO; ICP-OES results for metal loadings in N@rGO supports; state-of-the-art N-doping approaches on GO; EXAFS fitting parameters for Ni_N@rGO; state-of-the-art SA-N-C synthetic methods toward ORR applications (PDF)

AUTHOR INFORMATION

Corresponding Authors

Il-Doo Kim − *Department of Materials Science and Engineering, Korea Advanced Institute of Science and Technology (KAIST), Daejeon 34141, Republic of Korea; Membrane Innovation Center for Antivirus and Air-Quality Control, KAIST Institute Nanocentury, Daejeon 34141, Republic of Korea;* orcid.org/0000-0002-9970-2218; Email: idkim@kaist.ac.kr

Sung-Yool Choi − *School of Electrical Engineering and Center for Advanced Materials Discovery towards 3D Displays, Korea Advanced Institute of Science and Technology (KAIST), Daejeon 34141, Republic of Korea;* orcid.org/0000-0002-0960-7146; Email: sungyool.choi@kaist.ac.kr

Authors

Dong-Ha Kim − *Department of Materials Science and Engineering, Korea Advanced Institute of Science and Technology (KAIST), Daejeon 34141, Republic of Korea; Membrane Innovation Center for Antivirus and Air-Quality Control, KAIST Institute Nanocentury, Daejeon 34141, Republic of Korea;* Present Address: Department of Chemistry, Massachusetts Institute of Technology, 77 Massachusetts Avenue, Cambridge, Massachusetts 02139, United States

Jun-Hwe Cha − *School of Electrical Engineering and Center for Advanced Materials Discovery towards 3D Displays, Korea Advanced Institute of Science and Technology (KAIST), Daejeon 34141, Republic of Korea*

Sanggyu Chong − *Department of Chemical and Biomolecular Engineering, Korea Advanced Institute of Science and Technology (KAIST), Daejeon 34141, Korea;* orcid.org/0000-0002-6948-1602

Su-Ho Cho − *Department of Materials Science and Engineering, Korea Advanced Institute of Science and*

https://doi.org/10.1021/acsnano.3c02968
ACS Nano 2023, 17, 23347−23358

Technology (KAIST), Daejeon 34141, Republic of Korea; Membrane Innovation Center for Antivirus and Air-Quality Control, KAIST Institute Nanocentury, Daejeon 34141, Republic of Korea

Hamin Shin − *Department of Materials Science and Engineering, Korea Advanced Institute of Science and Technology (KAIST), Daejeon 34141, Republic of Korea; Membrane Innovation Center for Antivirus and Air-Quality Control, KAIST Institute Nanocentury, Daejeon 34141, Republic of Korea*

Jaewan Ahn − *Department of Materials Science and Engineering, Korea Advanced Institute of Science and Technology (KAIST), Daejeon 34141, Republic of Korea; Membrane Innovation Center for Antivirus and Air-Quality Control, KAIST Institute Nanocentury, Daejeon 34141, Republic of Korea;* orcid.org/0000-0002-0136-8427

Dogyeong Jeon − *Department of Materials Science and Engineering, Korea Advanced Institute of Science and Technology (KAIST), Daejeon 34141, Republic of Korea; Membrane Innovation Center for Antivirus and Air-Quality Control, KAIST Institute Nanocentury, Daejeon 34141, Republic of Korea*

Jihan Kim − *Department of Chemical and Biomolecular Engineering, Korea Advanced Institute of Science and Technology (KAIST), Daejeon 34141, Korea;* orcid.org/0000-0002-3844-8789

Complete contact information is available at: https://pubs.acs.org/10.1021/acsnano.3c02968

Author Contributions

D.-H.K. and J.-H.C. conceived the idea for this study. D.-H.K. synthesized the active materials, performed interpretations of XAFS and TEM analysis, and performed the gas sensing tests. J.-H.C. performed the IPL treatment, analysis of photothermal annealing temperature, and interpretation of X-ray photoelectron spectra. S.C. performed DFT simulation. S.-H.C. and D.J. conducted the electrochemical performance tests. H.S. performed interpretations of XAFS analysis. J.A. performed interpretation of TEM analysis. I.-D.K., S.-Y.C., and J.K. supervised the project and revised the manuscript. All authors commented on the data and the manuscript.

Author Contributions

$^{\nabla}$These authors contributed equally to this work.

Notes

The authors declare no competing financial interest.

ACKNOWLEDGMENTS

This work was supported by the National Research Foundation of Korea (NRF) grant funded by the Korea government, Ministry of Science and ICT (Grant No. 2020R1A2C301312711). This work was also supported by Nano Convergence Foundation funded by the Ministry of Science and ICT (MSIT, Korea) and the Ministry of Trade, Industry and Energy (MOTIE, Korea; No. 20000230). This work was also supported by grants from the Creative Materials Discovery Program through the National Research Foundation of Korea (NRF) funded by the Ministry of Science and ICT (NRF-2016M3D1A1900035).

REFERENCES

(1) Yang, X. F.; Wang, A. Q.; Qiao, B. T.; Li, J.; Liu, J. Y.; Zhang, T. Single-Atom Catalysts: A New Frontier in Heterogeneous Catalysis. *Acc. Chem. Res.* **2013**, *46*, 1740−1748.

(2) Wang, A. Q.; Li, J.; Zhang, T. Heterogeneous Single-Atom Catalysis. *Nat. Rev. Chem.* **2018**, *2*, 65−81.

(3) Qiao, B. T.; Wang, A. Q.; Yang, X. F.; Allard, L. F.; Jiang, Z.; Cui, Y. T.; Liu, J. Y.; Li, J.; Zhang, T. Single-Atom Catalysis of CO Oxidation Using Pt_1/FeO_x. *Nat. Chem.* **2011**, *3*, 634−641.

(4) Yin, P. Q.; Yao, T.; Wu, Y.; Zheng, L. R.; Lin, Y.; Liu, W.; Ju, H. X.; Zhu, J. F.; Hong, X.; Deng, Z. X.; Zhou, G.; Wei, S. Q.; Li, Y. D. Single Cobalt Atoms with Precise N-Coordination as Superior Oxygen Reduction Reaction Catalysts. *Angew. Chem., Int. Ed.* **2016**, *55*, 10800−10805.

(5) Cheng, N. C.; Stambula, S.; Wang, D.; Banis, M. N.; Liu, J.; Riese, A.; Xiao, B. W.; Li, R. Y.; Sham, T. K.; Liu, L. M.; Botton, G. A.; Sun, X. L. Platinum Single-Atom and Cluster Catalysis of the Hydrogen Evolution Reaction. *Nat. Commun.* **2016**, *7*, 13638.

(6) Shin, H.; Jung, W.-G.; Kim, D.-H.; Jang, J.-S.; Kim, Y. H.; Koo, W.-T.; Bae, J.; Park, C.; Cho, S.-H.; Kim, B. J.; Kim, I.-D. Single-Atom Pt Stabilized on One-Dimensional Nanostructure Support via Carbon Nitride/SnO_2 Heterojunction Trapping. *ACS Nano* **2020**, *14*, 11394−11405.

(7) Zeng, J.; Rong, Q.; Xiao, B.; Yu, R.; Zi, B.; Kuang, X.; Deng, X.; Ma, Y.; Zhang, J.; Wu, J.; Liu, Q. Single-Atom Silver Loaded on Tungsten Oxide with Oxygen Vacancies for High Performance Triethylamine Gas Sensors. *J. Mater. Chem. A* **2021**, *9*, 8704−8710.

(8) Lei, G.; Pan, H.; Mei, H.; Liu, X.; Lu, G.; Lou, C.; Li, Z.; Zhang, J. Emerging Single Atom Catalysts in Gas Sensors. *Chem. Soc. Rev.* **2022**, *51*, 7260.

(9) Zhang, Z.; Feng, C.; Liu, C.; Zuo, M.; Qin, L.; Yan, X.; Xing, Y.; Li, H.; Si, R.; Zhou, S.; Zeng, J. Electrochemical Deposition As a Universal Route for Fabricating Single-Atom Catalysts. *Nat. Commun.* **2020**, *11*, 1215.

(10) Wei, H.; Huang, K.; Wang, D.; Zhang, R.; Ge, B.; Ma, J.; Wen, B.; Zhang, S.; Li, Q.; Lei, M.; Zhang, C.; Irawan, J.; Liu, L.-M.; Wu, H. Iced Photochemical Reduction to Synthesize Atomically Dispersed Metals by Suppressing Nanocrystal Growth. *Nat. Commun.* **2017**, *8*, 1490.

(11) Bai, T.; Li, D.; Xiao, S.; Ji, F.; Zhang, S.; Wang, C.; Lu, J.; Gao, Q.; Ci, L. Recent Progress on Single Atom Catalysts for Lithium-air Battery Applications. *Energy Environ. Sci.* **2023**, *16*, 1431−1465.

(12) Xiong, H. F.; Datye, A. K.; Wang, Y. Thermally Stable Single-Atom Heterogeneous Catalysts. *Adv. Mater.* **2021**, *33*, 2004319.

(13) Peng, Y.; Lu, B. Z.; Chen, S. W. Carbon-Supported Single Atom Catalysts for Electrochemical Energy Conversion and Storage. *Adv. Mater.* **2018**, *30*, 1801995.

(14) Hai, X.; Xi, S. B.; Mitchell, S.; Harrath, K.; Xu, H. M.; Akl, D. F.; Kong, D. B.; Li, J.; Li, Z. J.; Sun, T.; Yang, H. M.; Cui, Y. G.; Su, C. L.; Zhao, X. X.; Li, J.; Perez-Ramirez, J.; Lu, J. Scalable Two-Step Annealing Method for Preparing Ultra-High-Density Single-Atom Catalyst Libraries. *Nat. Nanotechnol.* **2022**, *17*, 174−181.

(15) Bulushev, D. A.; Zacharska, M.; Lisitsyn, A. S.; Podyacheva, O. Y.; Hage, F. S.; Ramasse, Q. M.; Bangert, U.; Bulusheva, L. G. Single Atoms of Pt-Group Metals Stabilized by N-Doped Carbon Nanofibers for Efficient Hydrogen Production from Formic Acid. *ACS Catal.* **2016**, *6*, 3442−3451.

(16) Shin, H.; Ko, J.; Park, C.; Kim, D. H.; Ahn, J.; Jang, J. S.; Kim, Y. H.; Cho, S. H.; Baik, H.; Kim, I. D. Sacrificial Template-Assisted Synthesis of Inorganic Nanosheets with High-Loading Single-Atom Catalysts: A General Approach. *Adv. Funct. Mater.* **2022**, *32*, 2110485.

(17) Qu, Y. T.; Li, Z. J.; Chen, W. X.; Lin, Y.; Yuan, T. W.; Yang, Z. K.; Zhao, C. M.; Wang, J.; Zhao, C.; Wang, X.; Zhou, F. Y.; Zhuang, Z. B.; Wu, Y.; Li, Y. D. Direct Transformation of Bulk Copper into Copper Single Sites via Emitting and Trapping of Atoms. *Nat. Catal.* **2018**, *1*, 781−786.

(18) Zheng, T. T.; Jiang, K.; Ta, N.; Hu, Y. F.; Zeng, J.; Liu, J. Y.; Wang, H. T. Large-Scale and Highly Selective CO_2 Electrocatalytic Reduction on Nickel Single-Atom Catalyst. *Joule* **2019**, *3*, 265−278.

(19) Yang, H. Z.; Shang, L.; Zhang, Q. H.; Shi, R.; Waterhouse, G. I. N.; Gu, L.; Zhang, T. R. A Universal Ligand Mediated Method for Large Scale Synthesis of Transition Metal Single Atom Catalysts. *Nat. Commun.* **2019**, *10*, 4585.
(20) Han, G. F.; Li, F.; Rykov, A. I.; Im, Y. K.; Yu, S. Y.; Jeon, J. P.; Kim, S. J.; Zhou, W. H.; Ge, R.; Ao, Z. M.; Shin, T. J.; Wang, J. H.; Jeong, H. Y.; Baek, J. B. Abrading Bulk Metal into Single Atoms. *Nat. Nanotechnol.* **2022**, *17*, 403−407.
(21) Shi, W.; Li, Z.; Gong, Z.; Liang, Z.; Liu, H.; Han, Y.-C.; Niu, H.; Song, B.; Chi, X.; Zhou, J.; Wang, H.; Xia, B. Y.; Yao, Y.; Tian, Z.-Q. Transient and General Synthesis of High-Density and Ultrasmall Nanoparticles on Two-Dimensional Porous Carbon via Coordinated Carbothermal Shock. *Nat. Commun.* **2023**, *14*, 2294.
(22) Yao, Y. G.; Huang, Z. N.; Xie, P. F.; Lacey, S. D.; Jacob, R. J.; Xie, H.; Chen, F. J.; Nie, A. M.; Pu, T. C.; Rehwoldt, M.; Yu, D. W.; Zachariah, M. R.; Wang, C.; Shahbazian-Yassar, R.; Li, J.; Hu, L. B. Carbothermal Shock Synthesis of High-Entropy-Alloy Nanoparticles. *Science* **2018**, *359*, 1489−1494.
(23) Yao, Y.; Huang, Z.; Xie, P.; Wu, L.; Ma, L.; Li, T.; Pang, Z.; Jiao, M.; Liang, Z.; Gao, J.; He, Y.; Kline, D. J.; Zachariah, M. R.; Wang, C.; Lu, J.; Wu, T.; Li, T.; Wang, C.; Shahbazian-Yassar, R.; Hu, L. High Temperature Shockwave Stabilized Single Atoms. *Nat. Nanotechnol.* **2019**, *14*, 851−857.
(24) Dong, Q.; Hu, L. Shock Synthesis by Flash-Thermal Lamping. *Chem.* **2022**, *8*, 895.
(25) Kim, D.-H.; Cha, J.-H.; Shim, G.; Kim, Y. H.; Jang, J.-S.; Shin, H.; Ahn, J.; Choi, S.-Y.; Kim, I.-D. Flash-Thermochemical Engineering of Phase and Surface Activity on Metal Oxides. *Chem.* **2022**, *8*, 1014.
(26) Lin, K. T.; Lin, H.; Yang, T. S.; Jia, B. H. Structured Graphene Metamaterial Selective Absorbers for High Efficiency and Omnidirectional Solar Thermal Energy Conversion. *Nat. Commun.* **2020**, *11*, 1389.
(27) Zhang, Y. L.; Guo, L.; Xia, H.; Chen, Q. D.; Feng, J.; Sun, H. B. Photoreduction of Graphene Oxides: Methods, Properties, and Applications. *Adv. Opt. Mater.* **2014**, *2*, 10−28.
(28) Velasco-Soto, M. A.; Perez-Garcia, S. A.; Alvarez-Quintana, J.; Cao, Y.; Nyborg, L.; Licea-Jimenez, L. Selective Band Gap Manipulation of Graphene Oxide by its Reduction With Mild Reagents. *Carbon* **2015**, *93*, 967−973.
(29) Abid; Sehrawat, P.; Islam, S. S.; Mishra, P.; Ahmad, S. Reduced Graphene Oxide (rGO) Based Wideband Optical Sensor and the Role of Temperature, Defect States and Quantum Efficiency. *Sci. Rep.-Uk* **2018**, *8*, 3537.
(30) Chien, C. T.; Li, S. S.; Lai, W. J.; Yeh, Y. C.; Chen, H. A.; Chen, I. S.; Chen, L. C.; Chen, K. H.; Nemoto, T.; Isoda, S.; Chen, M. W.; Fujita, T.; Eda, G.; Yamaguchi, H.; Chhowalla, M.; Chen, C. W. Tunable Photoluminescence from Graphene Oxide. *Angew. Chem., Int. Ed.* **2012**, *51*, 6662−6666.
(31) Im, T. H.; Lee, J. H.; Wang, H. S.; Sung, S. H.; Kim, Y. B.; Rho, Y.; Grigoropoulos, C. P.; Park, J. H.; Lee, K. J. Flashlight-Material Interaction for Wearable and Flexible Electronics. *Mater. Today.* **2021**, *51*, 525−551.
(32) Fei, H. L.; Dong, J. C.; Feng, Y. X.; Allen, C. S.; Wan, C. Z.; Volosskiy, B.; Li, M. F.; Zhao, Z. P.; Wang, Y. L.; Sun, H. T.; An, P. F.; Chen, W. X.; Guo, Z. Y.; Lee, C.; Chen, D. L.; Shakir, I.; Liu, M. J.; Hu, T. D.; Li, Y. D.; Kirkland, A. I.; Duan, X. F.; Huang, Y. General Synthesis and Definitive Structural Identification of MN_4C_4 Single-Atom Catalysts with Tunable Electrocatalytic Activities. *Nat. Catal.* **2018**, *1*, 63−72.
(33) Guo, B. D.; Liu, Q. A.; Chen, E. D.; Zhu, H. W.; Fang, L. A.; Gong, J. R. Controllable N-Doping of Graphene. *Nano Lett.* **2010**, *10*, 4975−4980.
(34) Pei, S. F.; Cheng, H. M. The Reduction of Graphene Oxide. *Carbon* **2012**, *50*, 3210−3228.
(35) Cha, J. H.; Kim, D. H.; Park, C.; Choi, S. J.; Jang, J. S.; Yang, S. Y.; Kim, I.; Choi, S. Y. Low-Thermal-Budget Doping of 2D Materials in Ambient Air Exemplified by Synthesis of Boron-Doped Reduced Graphene Oxide. *Adv. Sci.* **2020**, *7*, 1903318.
(36) Sheng, Z. H.; Shao, L.; Chen, J. J.; Bao, W. J.; Wang, F. B.; Xia, X. H. Catalyst-Free Synthesis of Nitrogen-Doped Graphene via Thermal Annealing Graphite Oxide with Melamine and Its Excellent Electrocatalysis. *ACS Nano* **2011**, *5*, 4350−4358.
(37) Lin, Z. Y.; Song, M. K.; Ding, Y.; Liu, Y.; Liu, M. L.; Wong, C. P. Facile Preparation of Nitrogen-Doped Graphene as a Metal-Free Catalyst for Oxygen Reduction Reaction. *Phys. Chem. Chem. Phys.* **2012**, *14*, 3381−3387.
(38) Lai, L.; Potts, J. R.; Zhan, D.; Wang, L.; Poh, C. K.; Tang, C.; Gong, H.; Shen, Z.; Lin, J.; Ruoff, R. S. Exploration of the Active Center Structure of Nitrogen-Doped Graphene-Based Catalysts for Oxygen Reduction Reaction. *Energy Environ. Sci.* **2012**, *5*, 7936−7942.
(39) Fei, H.; Dong, J.; Arellano-Jimenez, M. J.; Ye, G.; Dong Kim, N.; Samuel, E. L.G.; Peng, Z.; Zhu, Z.; Qin, F.; Bao, J.; Yacaman, M. J.; Ajayan, P. M.; Chen, D.; Tour, J. M. Atomic Cobalt on Nitrogen-Doped Graphene for Hydrogen Generation. *Nat. Commun.* **2015**, *6*, 1−8.
(40) Han, L.; Cheng, H.; Liu, W.; Li, H.; Ou, P.; Lin, R.; Wang, H.-T.; Pao, C.-W.; Head, A. R.; Wang, C.-H.; Tong, X.; Sun, C.-J.; Pong, W.-F.; Luo, J.; Zheng, J.-C.; Xin, H. L. A Single-Atom Library for Guided Monometallic and Concentration-Complex Multimetallic Designs. *Nat. Mater.* **2022**, *21*, 681−688.
(41) Choi, S. J.; Kim, S. J.; Jang, J. S.; Lee, J. H.; Kim, I. D. Silver Nanowire Embedded Colorless Polyimide Heater for Wearable Chemical Sensors: Improved Reversible Reaction Kinetics of Optically Reduced Graphene Oxide. *Small* **2016**, *12*, 5826−5835.
(42) Mirzaei, A.; Bang, J. H.; Choi, M. S.; Han, S.; Lee, H. Y.; Kim, S. S.; Kim, H. W. Changes in Characteristics of Pt-Functionalized RGO Nanocomposites by Electron Beam Irradiation for Room Temperature NO_2 Sensing. *Ceram. Int.* **2020**, *46*, 21638−21646.
(43) Bo, Z.; Guo, X.; Wei, X.; Yang, H.; Yan, J.; Cen, K. Density Functional Theory Calculations of NO_2 and H_2S Adsorption on the Group 10 Transition Metal (Ni, Pd and Pt) Decorated Graphene. *Phys. E: Low-Dimens. Syst.* **2019**, *109*, 156−163.
(44) Shao, M. H.; Chang, Q. W.; Dodelet, J. P.; Chenitz, R. Recent Advances in Electrocatalysts for Oxygen Reduction Reaction. *Chem. Rev.* **2016**, *116*, 3594−3657.
(45) Lee, C. Y.; Strano, M. S. Understanding the Dynamics of Signal Transduction for Adsorption of Gases and Vapors on Carbon Nanotube Sensors. *Langmuir* **2005**, *21*, 5192−5196.
(46) Xu, S. C.; Kim, Y.; Higgins, D.; Yusuf, M.; Jaramillo, T. F.; Prinz, F. B. Building Upon the Koutecky-Levich Equation for Evaluation of Next-Generation Oxygen Reduction Reaction Catalysts. *Electrochim. Acta* **2017**, *255*, 99−108.

https://doi.org/10.1021/acsnano.3c02968
ACS Nano 2023, 17, 23347−23358